Electronic Supplementary Material (ESI) for Physical Chemistry Chemical Physics.

Supplementary Information

Activity and Stability Trends of Perovskite Oxides at Neutral pH for Oxygen Evolution Catalysis

Binghong Han,[a,c‡] *Marcel Risch,*[b,c‡] *Yueh-Lin Lee,*[b,c] *Chen Ling,*[d] *Hongfei Jia,*[d] *Yang Shao-Horn*[a,b,c*]

[a]Department of Materials Science and Engineering, [b]Research Laboratory of Electronics, and [c]Electrochemical Energy Lab, Massachusetts Institute of Technology, Cambridge, Massachusetts 02139, United States

[d]Toyota Research Institute of North America, Ann Arbor, Michigan 48105, United States

Corresponding Author

* Yang Shao-Horn, shaohorn@mit.edu

Index   Page

Detailed Experimental Section

Supporting Figures

Detailed Experimental Section

Materials Preparation. Perovskite catalysts were synthesized using a conventional solid-state route.[1] IrO_2 (99.99%) were bought from Alfa Aesar Premion as the precious-metal oxides reference. The specific surface area of each oxide sample was determined using BET analysis on a Quantachrome ChemBET Pulsar from a single-point BET analysis performed after 12 h outgassing at 150 C.

Electrochemical Measurements. The rotating disk electrode (RDE) configuration was employed for electrochemical measurements, which has a rotatable working electrode at the rotation speed of 1600 rpm in a three-electrode cell with a Pt wire and a saturated calomel electrode (Pine Instrument Co.) as the counter and reference electrodes, respectively. All potentials were calibrated to the reversible hydrogen electrode (RHE) using H_2/H^+ redox. Working electrodes were prepared by drop-casting oxide ink on a glassy carbon electrode, as described previously[1], with an oxide loading of 0.25 mg_{oxide}/cm^2_{disk} and a mass ratio of 5:1:1 of oxide catalyst to acetylene black carbon to Nafion® . The pH 13 electrolyte was prepared with 0.1 M KOH (Sigma-Aldrich, 99.99%) and deionized water (18 MΩ). pH 7 electrolyte was prepared with 0.4 M NaH_2PO_4 (Sigma-Aldrich), 0.6 M Na_2SO_4 (Sigma-Aldrich), proper amount of NaOH (Mallinckrodt) and deionized water (18 MΩ). The potential was controlled using a Biologic VSP-300 potentiostat. A scan rate of 10 mV/s and a scan range between 1.1 and 1.8 V vs. RHE were used for all CV measurements. All CV, galvanostatic and potentiostatic OER measurements were done in O_2 (99.999%, Airgas) saturated and bubbled electrolyte. Error bars in all activity data represent the standard deviation of multiple independent measurements. Ohmic losses were corrected by subtracting the ohmic voltage drop from the measured potential, using an electrolyte resistance determined by high-frequency alternating current impedance, where iR-corrected potentials are denoted as E-iR (i as the current and R as the electrolyte resistance). The resistance of the RDE system with pH 7 electrolyte (~15 Ω) is smaller than that with pH 13 electrolyte (~40 Ω), and therefore the Ohmic drop within the narrow pores[2] might not be a reason for the activity reduction observed at pH 7.

Transmission Electron Microscopy. TEM samples were prepared by dropping the catalyst ink onto Cu grids or using grids to scratch the working electrode after OER measurements. TEM images in this work were taken on JEOL 2010F equipped with ultrahigh resolution polepiece, having a point resolution of 0.19 nm. Bright field diffraction contrast imaging was used to determine particle size distributions and general morphology of the catalyst nanoparticles. The digital images were analyzed using Gatan Digital Micrograph v2.01 (Gatan Inc.) and ImageJ v1.44p (National Institute of Health, USA). High resolution TEM (HRTEM) images were formed without an objective aperture and were analyzed using Gatan Digital Micrograph. Parallel-beam energy dispersive spectroscopy (EDS) data were collected and the atomic compositions were determined using INCA (Oxford Instruments) software. For each oxides sample, three different spots with a diameter of ~ 200 nm were used to collect the bulk chemical composition, while three different spots with a diameter of ~ 5 nm at the particle edges were used to collect the surface chemical composition. Error bars in all EDS data represent the standard deviation of the results on multiple spots.

Density Function Theory studies. Spin polarized DFT calculations of the oxygen p-band center were performed with the Vienna Ab-initio Simulation Package (VASP)[3] using a plane wave basis set, the GGA-Perdew-Wang-91[4] exchange correlation function, and the Projector Augmented Wave (PAW) method.[5] We used PAW potentials with electronic configurations La (5s2 5p6 6s2 5d1), Sr (5s2 4p6), O_s (soft oxygen pseudopotential, 2s2 2p4), B = Mn_{pv} (3p6 3d6 4s1), Fe_{pv} (3p6 3d7 4s1), Co (3d8 4s1), and Ni_{pv} (3p6 3d9 4s1). All calculations were performed with an energy cut-off of 450 eV. For the GGA+U calculation, we used the standard Dudarev implementation[6], where the on-site Coulomb interaction for the localized transition metal d orbitals was parametrized by $U_{eff} = U - J$ with the Perdew-Wang-91 functional. Optimized U_{eff} for the transition metal atoms in the investigated perovskite systems (U_{eff} = 4.0, 4.0, 3.3, and 6.4 eV for Mn, Fe, Co and Ni, respectively) were taken from References.[7, 8] Full optimization of bulk 2×2×2 perovskite supercell calculations were performed using the experimental symmetry at low temperature[9] based on the ferromagnetic ordering in order to use a consistent and tractable set of magnetic structures using a (2×2×2) k-point mesh. An effective O p-band center of each perovskite systems was determined by taking the centroid of the projected density of states of O 2p states relative to the Fermi level.

The leaching reaction energies of $LaCoO_3$ in Figure 5 of the main text were also calculated with the same DFT approach described above. The electrochemical reactions of the dissolution process on working electrode can be written as:

$$LaCoO_3 \rightarrow La_{1-x}CoO_3 + x \cdot La_{aq}^{3+} + 3x \cdot e^- \quad \text{Eq. S1}$$

and

$$LaCoO_3 + yz \cdot H_2O \rightarrow LaCo_{1-y}O_3 + y \cdot CoO_z + 2yz \cdot H^+ + 2yz \cdot e^- \quad \text{Eq. S2}$$

for La and Co leaching, respectively. At the same time, there is other half-cell reaction to balance the chemical reaction in the DFT calculation, which could be written as:

$$O_2 + 4H^+ + 4e^- \rightarrow 2H_2O \quad \text{Eq. S3}$$

It is worth noticing here that the influential factor in A-site and B-site leaching mechanisms is the competition between Eq. S1 and S2 as well as the OER on the working electrode, and the compensation half-cell reaction (Eq. S3) has little influence to the degradation of the perovskite oxides on the working electrodes. Here Eq. S3 is just used to complete the whole reaction for DFT calculation, altering the voltage shifts to the oxygen chemical potential change. The real counter electrode reaction could be other forms of oxygen reduction (such as that in high pH involving OH^- rather than H^+) or even other redox reactions, but it won’t influence our conclusion. In the case of Eq. S3, the overall reactions for the DFT calculation can be obtained by combining Eq. S1 and S2 with Eq. S3:

$$\mathrm{LaCoO_3} + 3x \cdot H^{+} + \frac{3x}{4}\mathrm{O_2} \rightarrow \mathrm{La_{1-x}CoO_3} + x \cdot La_{aq}^{3+} + \frac{3x}{2}\mathrm{H_2}O$$

$$\mathrm{LaCoO_3} + \frac{zy}{2}\mathrm{O_2} \rightarrow \mathrm{LaCo_{1-y}O_3} + y \cdot \mathrm{Co}O_z$$

which are Eq. 1 and Eq. 2 in the main text, respectively.
The simulated $LaCoO_3$ bulk structures with 0.125, 0.25, 0.375, and 0.5 concentration of A-site or B-site vacancy in the 2×2×2 perovskite supercells are provided in Figure S14. The corresponding chemical potential of oxygen a given potential relative to the standard hydrogen electrode (SHE), $\mu(O)$, were computed following the computational SHE method[10, 11] and can be defined as:

$$\mu(O) = \left[E_{DFT}(H_2O^{(g)}) + ZPE_{H_2O} - TS^0_{H_2O^{(g)}}(0.035bar)\right]$$

$$-\left[E_{DFT}(H_2^{(g)} + ZPE_{H_2} - TS^0_{H_2^{(g)}}\right] + 2\left(k_b T \ln a_{H^+} - e\phi\right)$$

where $E_{DFT}\left(H_2O^{(g)}\right)$ and $E_{DFT}(H_2^{(g)})$ are the calculated DFT energy of gas phase H_2O and H_2, $ZPE_{H_2O}(ZPE_{H_2})$ and $S^0_{H_2O^{(g)}}$($S^0_{H_2^{(g)}}$) are the zero point energy and entropy of H_2O (H_2), respectively, T is the room temperature, and ϕ is the applied potential. The stability of solvated La^{3+} (assumed to be at 10^{-6} M concentration[12, 13]) was assessed by referencing to the experimental formation enthalpy of La_2O_3 (-18.58 eV per formula unit[14]) based on the reaction free energy of $1/2La_2O_3 + 3H^+ \rightarrow La^{3+} + 3/2H_2O$, and the calculated DFT total energy of La_2O_3 is used to align with the experimental La_2O_3 formation enthalpy.

The stable degradation product of Co-loss reaction was assumed to be CoO_z (z=4/3, 3/2, and 2, and the most stable compound among the three at the applied potential condition vs. RHE will be used in the Co-loss reaction) as a sufficient criteria for the Co-loss reaction. The extreme oxidative condition studied in this paper, especially at 2.33 V vs. RHE, other Co species, such as Co(IV)-oxo and $CoO_m(OH)_n$, might also be the direct or second-step product of Co-loss reaction.[15-17], but here we only focus on the stable CoO_z product. We note even if $CoO_m(OH)_n$ or other Co species are more stable than CoO_z, it will just further increase the actual driving force of the oxide Co leaching reaction, and has limited influence to the conclusions. Therefore, we hold the calculation of Co-loss reaction only with CoO_z. Here multiple z values were tried from 4/3 to 2 to find the most stable Co oxides under different voltage. Our calculation showed that at 1.23 V vs. RHE, z = 4/3; while at 1.75 and 2.33 V vs. RHE, z = 2.

Supporting Figures

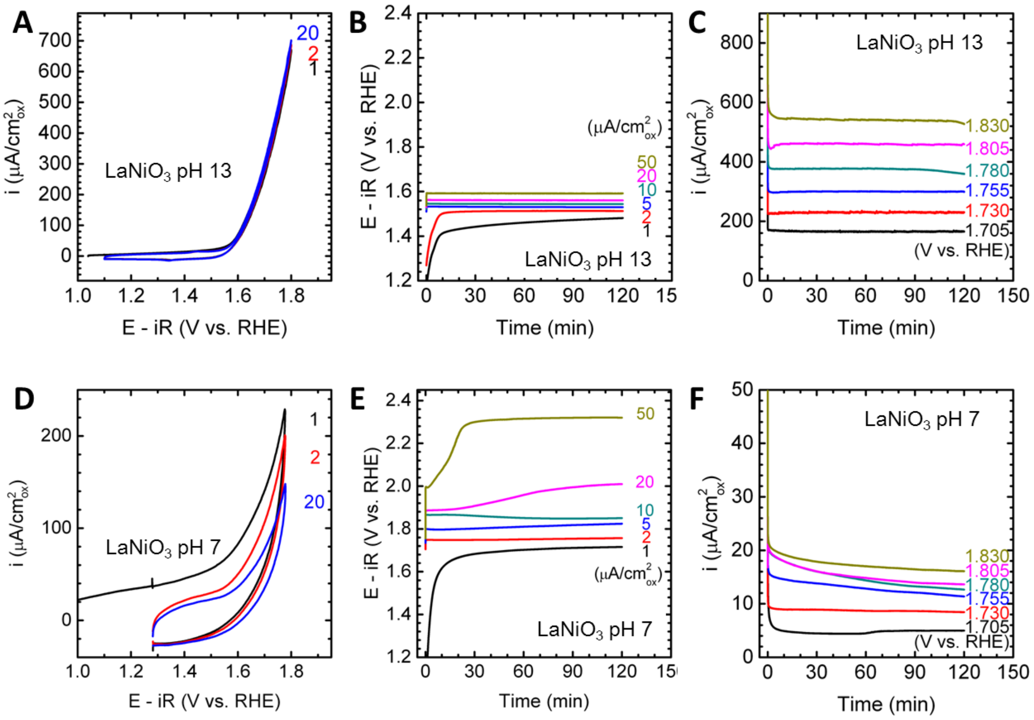

Figure S1. Electrochemical measurements of the $LaNiO_3$ OER activity. (A)(D) Cyclic voltammetry. Numbers indicate cycles. (B)(E) Galvanostatic experiments at various current densities. (C)(F) Potentiostatic experiments at various voltages. (A)-(C) was measured at pH 13, while (D)-(F) was measured at pH 7.

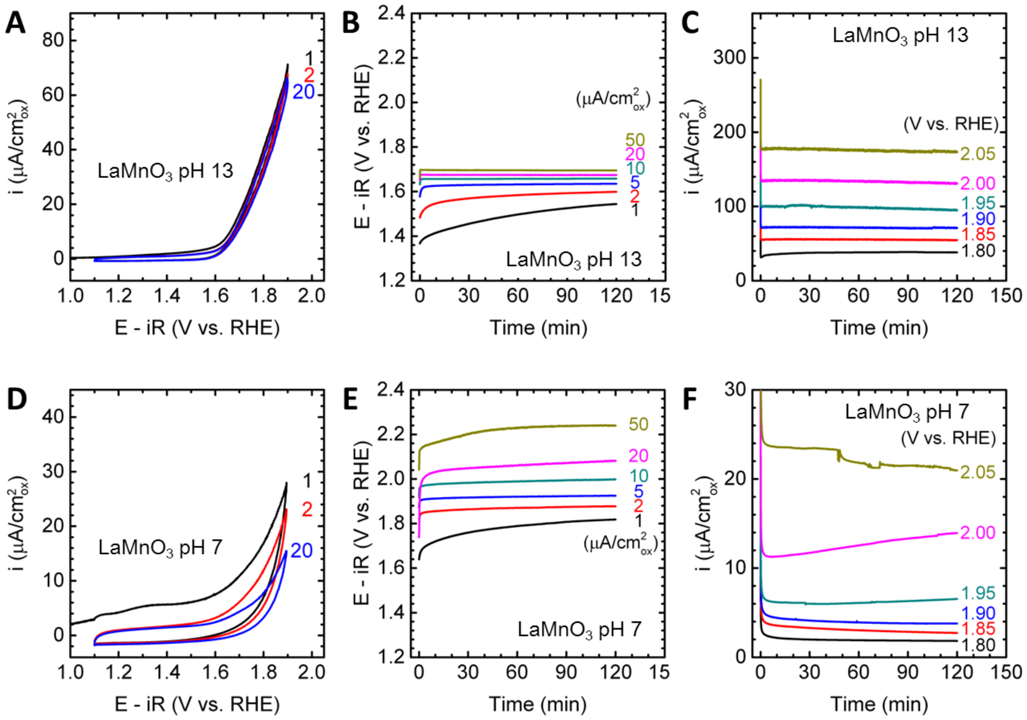

Figure S2. Electrochemical measurements of the $LaMnO_3$ OER activity. (A)(D) Cyclic voltammetry. Numbers indicate cycles. (B)(E) Galvanostatic experiments at various current densities. (C)(F) Potentiostatic experiments at various voltages. (A)-(C) was measured at pH 13, while (D)-(F) was measured at pH 7.

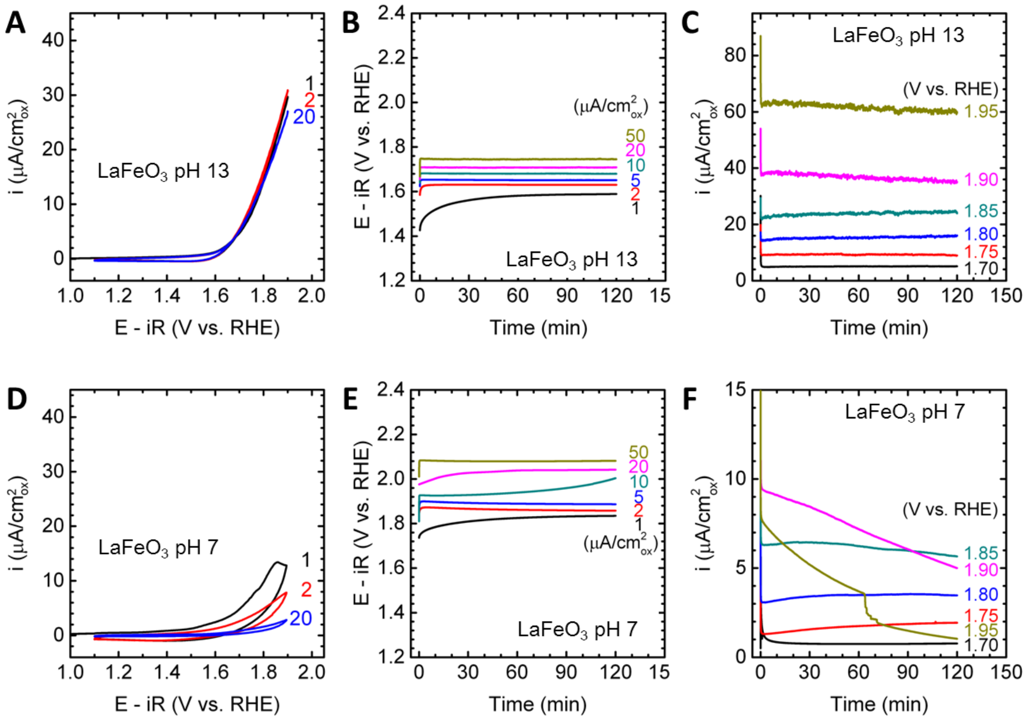

Figure S3. Electrochemical measurements of the LaFeO$_3$ OER activity. (A)(D) Cyclic voltammetry. Numbers indicate cycles. (B)(E) Galvanostatic experiments at various current densities. (C)(F) Potentiostatic experiments at various voltages. (A)-(C) was measured at pH 13, while (D)-(F) was measured at pH 7.

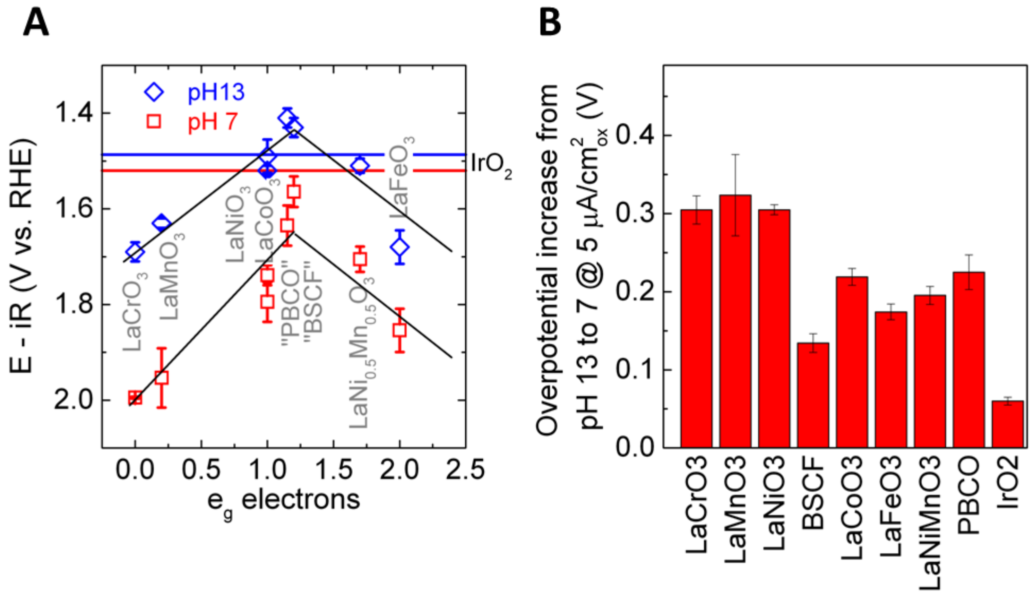

Figure S4. (A) OER activity vs. e_g electron filling at 5 μA/cm^2_{ox} under pH 7 and 13. Two "volcano plots" can be found, with much lower activities at pH 7. Those materials with quotation marks in the names are the catalysts that are not stable at 5 μA/cm^2_{ox} at pH 7. The horizontal lines represent the activity of IrO_2 at 5 μA/cm^2_{ox}. The black lines are only for eye guidance. (B) The OER overpotential increase from pH 13 to pH 7 at 5 μA/cm^2_{ox}. All error bars represent the standard deviation of multiple measurements.

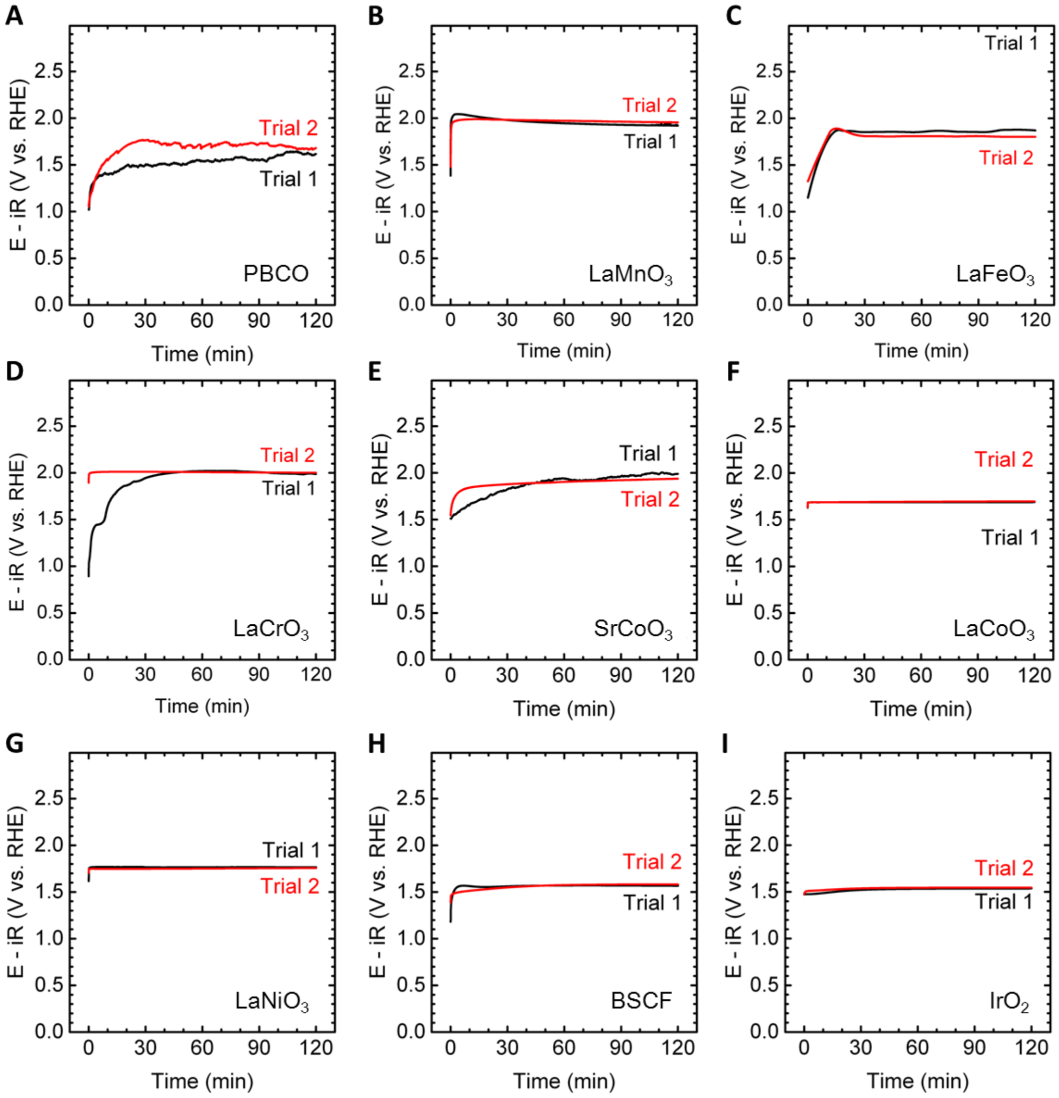

Figure S5. OER activity at pH 7 at 5 $\mu A/cm^2_{oxides}$ of (A) PBCO (B) $LaMnO_3$ (C) $LaFeO_3$ (D) $LaCrO_3$ (E) $SrCoO_3$ (F) $LaCoO_3$ (G) $LaNiO_3$ (H) BSCF (I) IrO_2

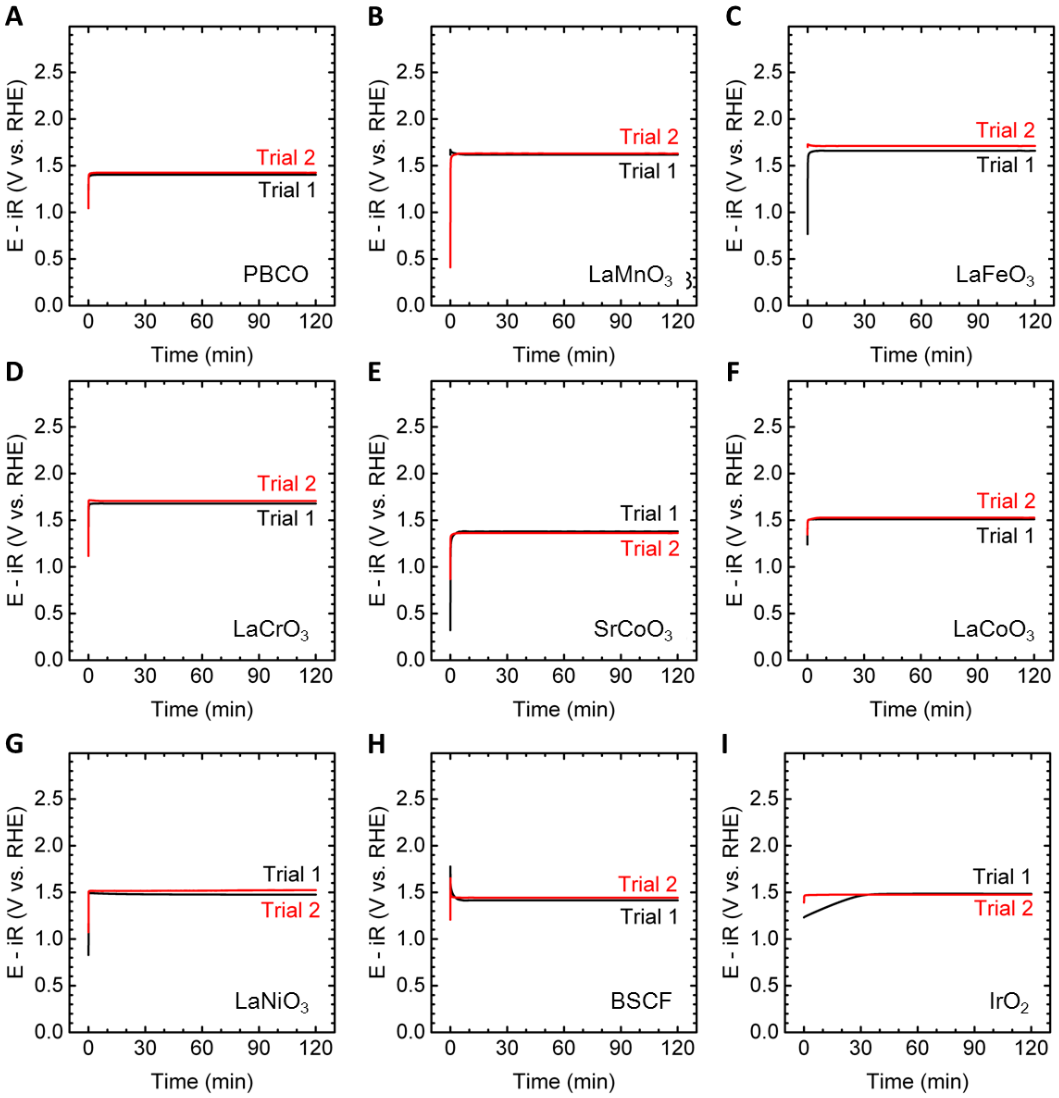

Figure S6. OER activity at pH 13 at 5 μA/cm$^2_{\text{oxides}}$ of (A) PBCO (B) $LaMnO_3$ (C) $LaFeO_3$ (D) $LaCrO_3$ (E) $SrCoO_3$ (F) $LaCoO_3$ (G) $LaNiO_3$ (H) BSCF (I) IrO_2

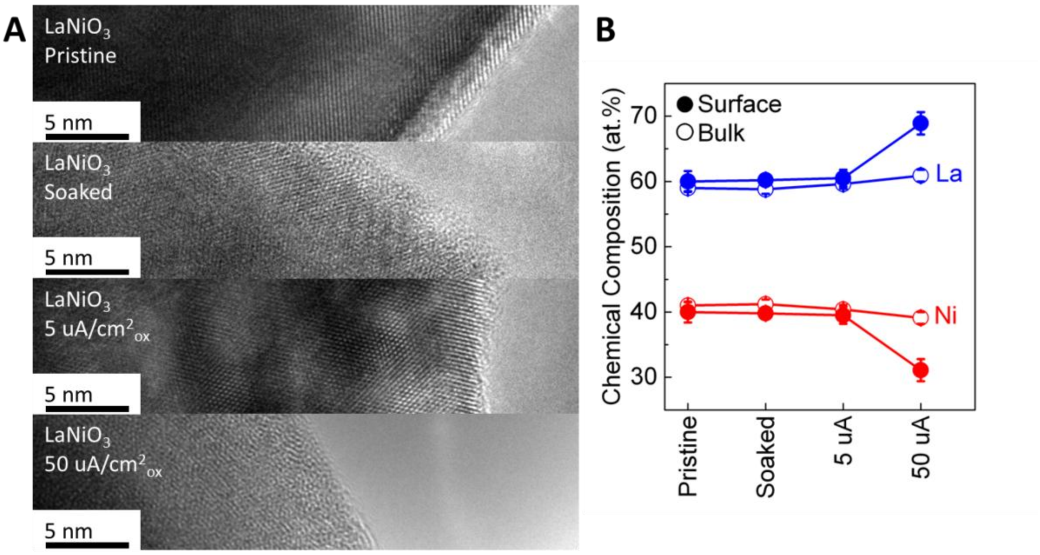

Figure S7. (A) TEM images and (B) EDS-determined chemical compositions of $LaNiO_3$ in pristine state, operated at 0 (soaking), 5 and 50 μA/cm^2_{ox} for 2 h at pH 7. The error bars in (B) represent the standard deviation of multiple spots.

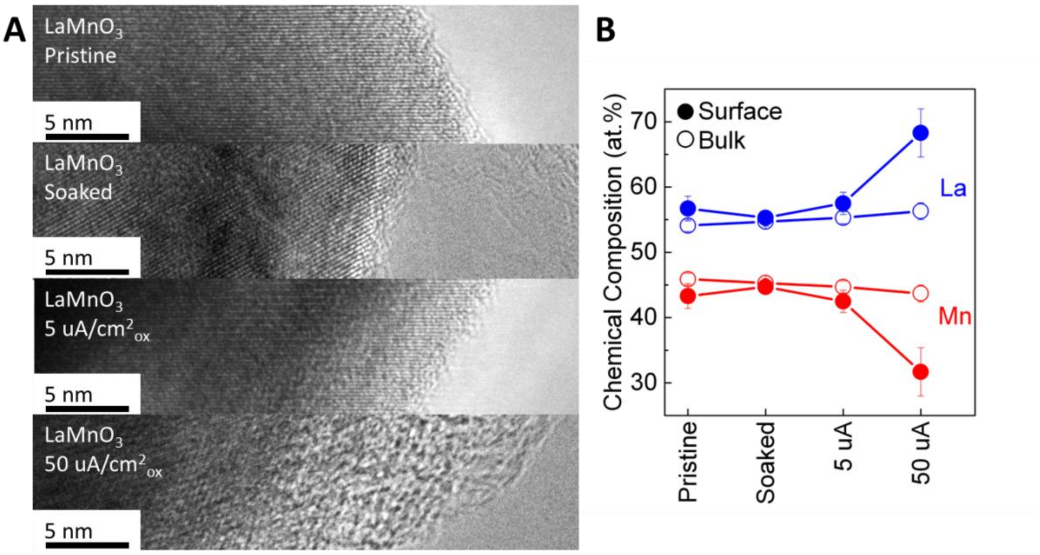

Figure S8. (A) TEM images and (B) EDS-determined chemical compositions of $LaMnO_3$ in pristine state, operated at 0 (soaking), 5 and 50 μA/cm^2_{ox} for 2 h at pH 7. The error bars in (B) represent the standard deviation of multiple spots.

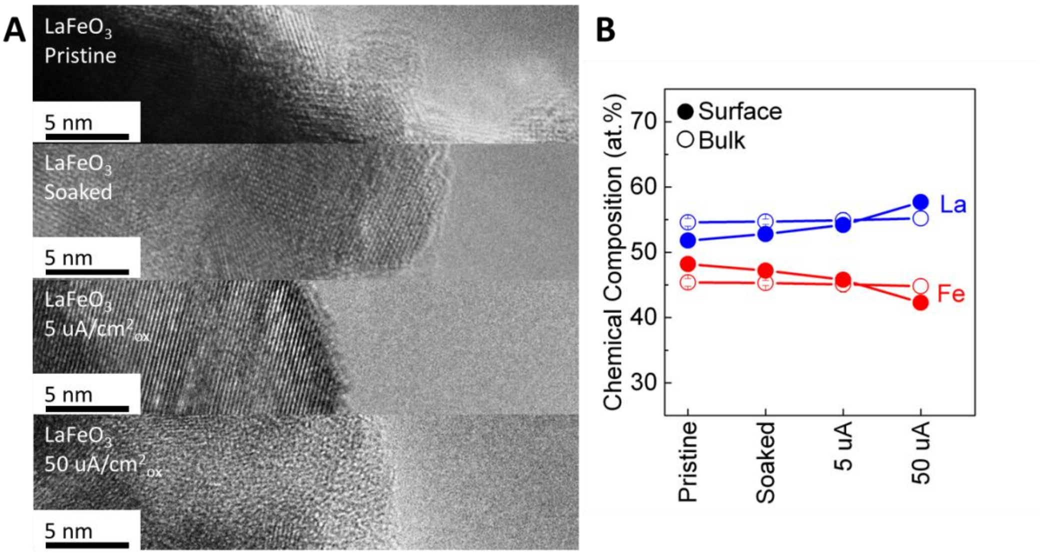

Figure S9. (A) TEM images and (B) EDS-determined chemical compositions of $LaFeO_3$ in pristine state, operated at 0 (soaking), 5 and 50 μA/cm^2_{ox} for 2 h at pH 7. The error bars in (B) represent the standard deviation of multiple spots.

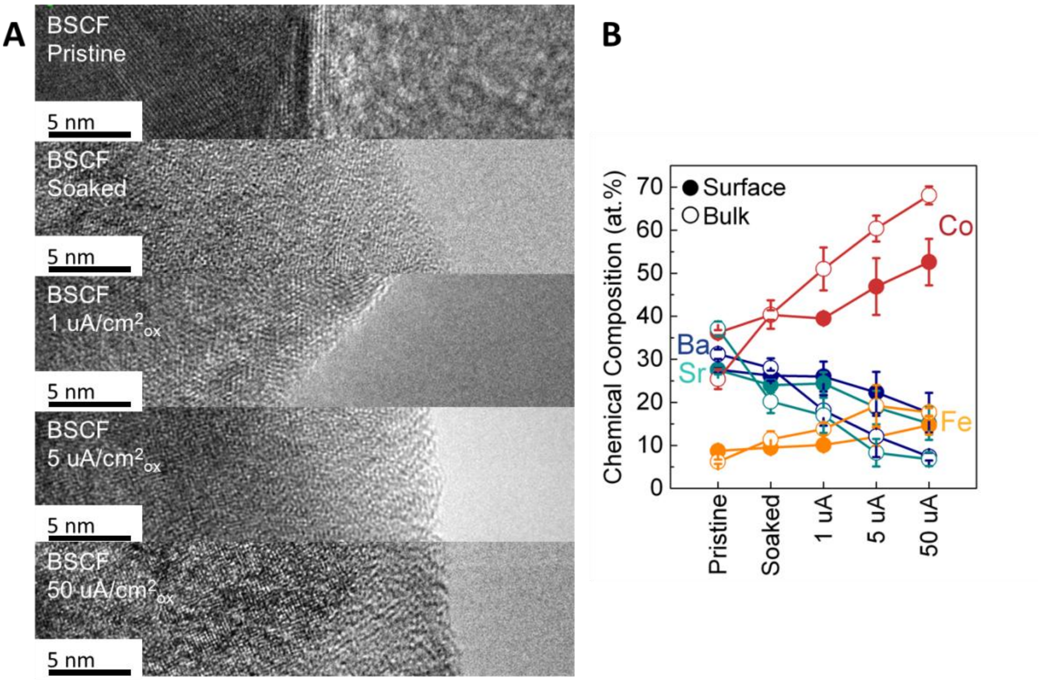

Figure S10. (A) TEM images and (B) EDS-determined chemical compositions of BSCF in pristine state, operated at 0 (soaking), 1, 5 and 50 μA/cm^2_{ox} for 2 h at pH 7. The error bars in (B) represent the standard deviation of multiple spots.

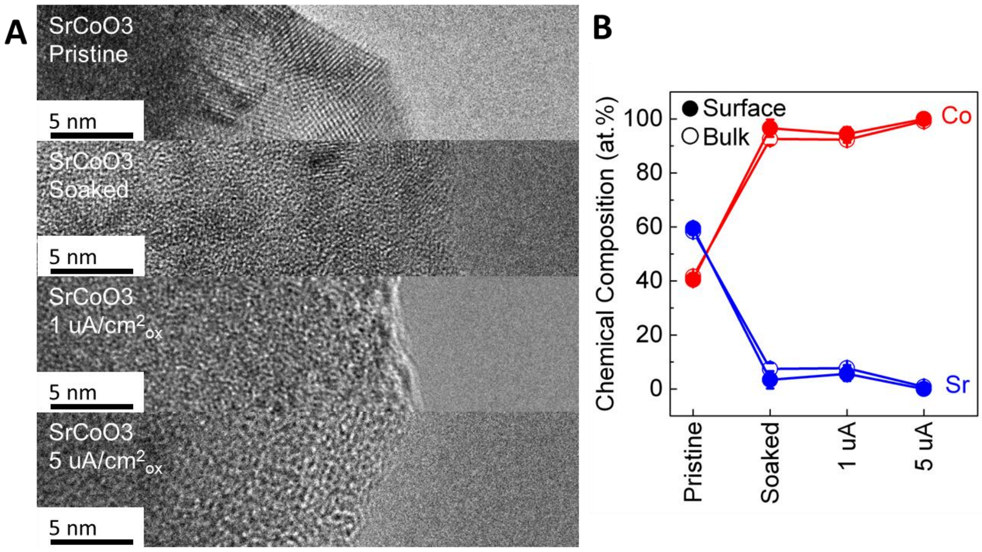

Figure S11. (A) TEM images and (B) EDS-determined chemical compositions of $SrCoO_3$ in pristine state, operated at 0 (soaking), 1 and 5 μA/cm$^2_{ox}$ for 2 h at pH 7. The error bars in (B) represent the standard deviation of multiple spots.

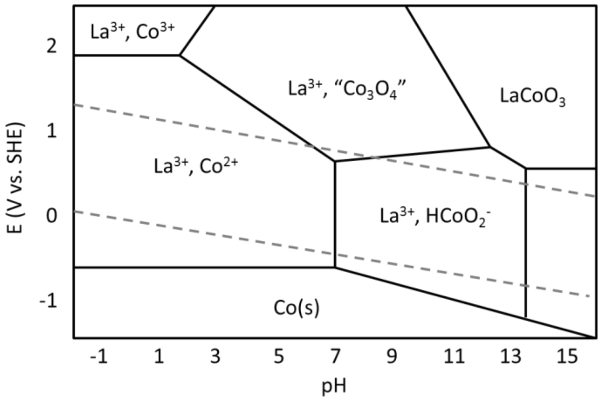

Figure S12. Pourbaix diagram of the Co-La-O(H) system predicted by DFT (data from materialsproject.org). Dashed lines indicate H_2/H^+ and H_2O/O_2. Co and La cation concentrations were assumed to be 10^{-6} M in the electrolytes.

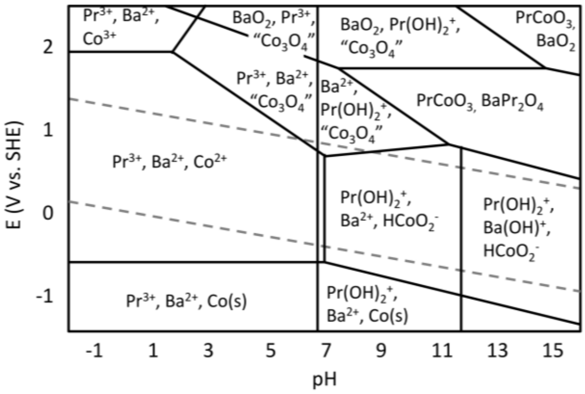

Figure S13. Pourbaix diagram of the Pr-Ba-Co-O(H) system predicted by DFT (data from materialsproject.org). Dashed lines indicate H_2/H^+ and H_2O/O_2. Pr, Co and Ba cation concentrations were assumed to be 10^{-6} M in the electrolytes.

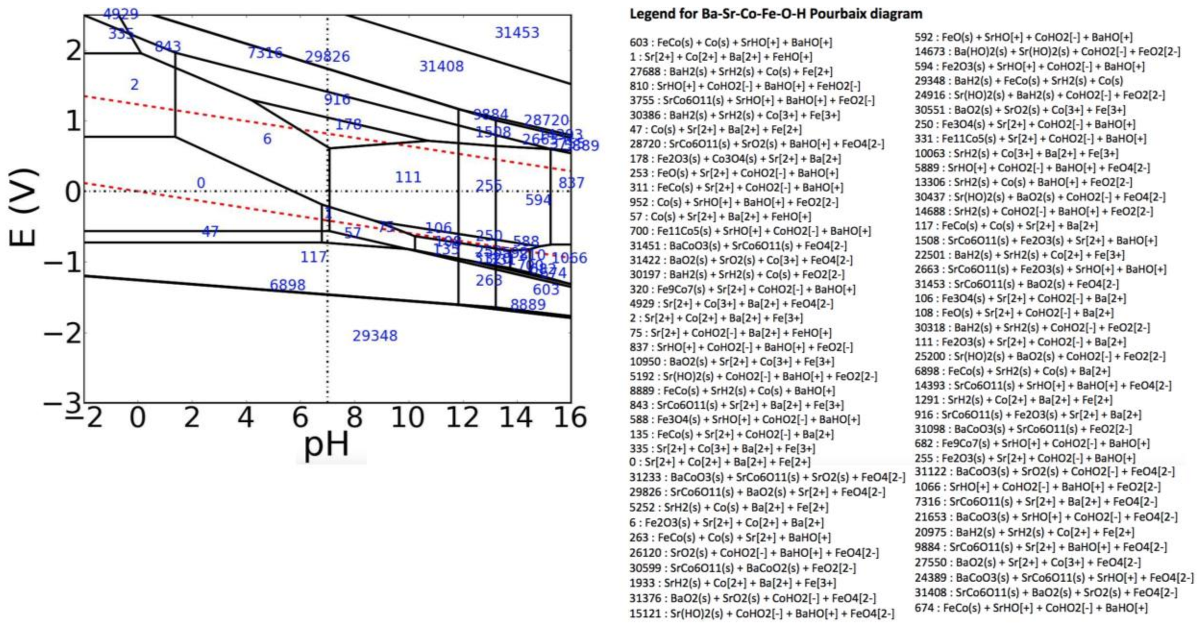

Legend for Ba-Sr-Co-Fe-O-H Pourbaix diagram

603 : FeCo(s) + Co(s) + SrHO[+] + BaHO[+]
1 : Sr[2+] + Co[2+] + Ba[2+] + FeHO[+]
27688 : BaH2(s) + SrH2(s) + Co(s) + Fe[2+]
810 : SrHO[+] + CoHO2[-] + BaHO[+] + FeHO2[-]
3755 : SrCo6O11(s) + SrHO[+] + BaHO[+] + FeO2[-]
30386 : BaH2(s) + SrH2(s) + Co[3+] + Fe[3+]
47 : Co(s) + Sr[2+] + Ba[2+] + Fe[2+]
28720 : SrCo6O11(s) + SrO2(s) + BaHO[+] + FeO4[2-]
178 : Fe2O3(s) + Co3O4(s) + Sr[2+] + Ba[2+]
253 : FeO(s) + Sr[2+] + CoHO2[-] + BaHO[+]
311 : FeCo(s) + Sr[2+] + CoHO2[-] + BaHO[+]
952 : Co(s) + SrHO[+] + BaHO[+] + FeO2[2-]
57 : Co(s) + Sr[2+] + Ba[2+] + FeHO[+]
700 : Fe11Co5(s) + SrHO[+] + CoHO2[-] + BaHO[+]
31451 : BaCoO3(s) + SrCo6O11(s) + FeO4[2-]
31422 : BaO2(s) + SrO2(s) + Co[3+] + FeO4[2-]
30197 : BaH2(s) + SrH2(s) + Co(s) + FeO2[2-]
320 : Fe9Co7(s) + Sr[2+] + CoHO2[-] + BaHO[+]
4929 : Sr[2+] + Co[3+] + Ba[2+] + FeO4[2-]
2 : Sr[2+] + Co[2+] + Ba[2+] + Fe[3+]
75 : Sr[2+] + CoHO2[-] + Ba[2+] + FeHO[+]
837 : SrHO[+] + CoHO2[-] + BaHO[+] + FeO2[-]
10950 : BaO2(s) + Sr[2+] + Co[3+] + Fe[3+]
5192 : Sr(HO)2(s) + CoHO2[-] + BaHO[+] + FeO2[2-]
8889 : FeCo(s) + SrH2(s) + Co(s) + BaHO[+]
843 : SrCo6O11(s) + Sr[2+] + Ba[2+] + Fe[3+]
588 : Fe3O4(s) + SrHO[+] + CoHO2[-] + BaHO[+]
135 : FeCo(s) + Sr[2+] + CoHO2[-] + Ba[2+]
335 : Sr[2+] + Co[3+] + Ba[2+] + Fe[3+]
0 : Sr[2+] + Co[2+] + Ba[2+] + Fe[2+]
31233 : BaCoO3(s) + SrCo6O11(s) + SrO2(s) + FeO4[2-]
29826 : SrCo6O11(s) + BaO2(s) + Sr[2+] + FeO4[2-]
5252 : SrH2(s) + Co(s) + Ba[2+] + Fe[2+]
6 : Fe2O3(s) + Sr[2+] + Co[2+] + Ba[2+]
263 : FeCo(s) + Co(s) + Sr[2+] + BaHO[+]
26120 : SrO2(s) + CoHO2[-] + BaHO[+] + FeO4[2-]
30599 : SrCo6O11(s) + BaCoO2(s) + FeO2[2-]
1933 : SrH2(s) + Co[2+] + Ba[2+] + Fe[3+]
31376 : BaO2(s) + SrO2(s) + CoHO2[-] + FeO4[2-]
15121 : Sr(HO)2(s) + CoHO2[-] + BaHO[+] + FeO4[2-]
592 : FeO(s) + SrHO[+] + CoHO2[-] + BaHO[+]
14673 : Ba(HO)2(s) + Sr(HO)2(s) + CoHO2[-] + FeO2[2-]
594 : Fe2O3(s) + SrHO[+] + CoHO2[-] + BaHO[+]
29348 : BaH2(s) + FeCo(s) + SrH2(s) + Co(s)
24916 : Sr(HO)2(s) + BaH2(s) + CoHO2[-] + FeO2[2-]
30551 : BaO2(s) + SrO2(s) + Co[3+] + Fe[3+]
250 : Fe3O4(s) + Sr[2+] + CoHO2[-] + BaHO[+]
331 : Fe11Co5(s) + Sr[2+] + CoHO2[-] + BaHO[+]
10063 : SrH2(s) + Co[3+] + Ba[2+] + Fe[3+]
5889 : SrHO[+] + CoHO2[-] + BaHO[+] + FeO4[2-]
13306 : SrH2(s) + Co(s) + BaHO[+] + FeO2[2-]
30437 : Sr(HO)2(s) + BaO2(s) + CoHO2[-] + FeO4[2-]
14688 : SrH2(s) + CoHO2[-] + BaHO[+] + FeO2[2-]
117 : FeCo(s) + Co(s) + Sr[2+] + Ba[2+]
1508 : SrCo6O11(s) + Fe2O3(s) + Sr[2+] + BaHO[+]
22501 : BaH2(s) + SrH2(s) + Co[2+] + Fe[3+]
2663 : SrCo6O11(s) + Fe2O3(s) + SrHO[+] + BaHO[+]
31453 : SrCo6O11(s) + BaO2(s) + FeO4[2-]
106 : Fe3O4(s) + Sr[2+] + CoHO2[-] + Ba[2+]
108 : FeO(s) + Sr[2+] + CoHO2[-] + Ba[2+]
30318 : BaH2(s) + SrH2(s) + CoHO2[-] + FeO2[2-]
111 : Fe2O3(s) + Sr[2+] + CoHO2[-] + Ba[2+]
25200 : Sr(HO)2(s) + BaO2(s) + CoHO2[-] + FeO2[2-]
6898 : FeCo(s) + SrH2(s) + Co(s) + Ba[2+]
14393 : SrCo6O11(s) + SrHO[+] + BaHO[+] + FeO4[2-]
1291 : SrH2(s) + Co[2+] + Ba[2+] + Fe[2+]
916 : SrCo6O11(s) + Fe2O3(s) + Sr[2+] + Ba[2+]
31098 : BaCoO3(s) + SrCo6O11(s) + FeO2[2-]
682 : Fe9Co7(s) + SrHO[+] + CoHO2[-] + BaHO[+]
255 : Fe2O3(s) + Sr[2+] + CoHO2[-] + BaHO[+]
31122 : BaCoO3(s) + SrO2(s) + CoHO2[-] + FeO4[2-]
1066 : SrHO[+] + CoHO2[-] + BaHO[+] + FeO2[2-]
7316 : SrCo6O11(s) + Sr[2+] + Ba[2+] + FeO4[2-]
21653 : BaCoO3(s) + SrHO[+] + CoHO2[-] + FeO4[2-]
20975 : BaH2(s) + SrH2(s) + Co[2+] + Fe[2+]
9884 : SrCo6O11(s) + Sr[2+] + BaHO[+] + FeO4[2-]
27550 : BaO2(s) + Sr[2+] + Co[3+] + FeO4[2-]
24389 : BaCoO3(s) + SrCo6O11(s) + SrHO[+] + FeO4[2-]
31408 : SrCo6O11(s) + BaO2(s) + SrO2(s) + FeO4[2-]
674 : FeCo(s) + SrHO[+] + CoHO2[-] + BaHO[+]

Figure S14. Pourbaix diagram of the Ba-Sr-Co-Fe-Co-O(H) system predicted by DFT (data from Ryan Jacobs). Dashed lines indicate H_2/H^+ and H_2O/O_2. Fe, Sr and Co cation concentrations were assumed to be 10^{-6} M in the electrolytes.

References

1. A. Grimaud, K. J. May, C. E. Carlton, Y.-L. Lee, M. Risch, W. T. Hong, J. Zhou and Y. Shao-Horn, *Nat. Commun.*, 2013, **4**, 2439 2431-2437.
2. L. Bai, L. Gao and B. E. Conway, *Journal of the Chemical Society, Faraday Transactions*, 1993, **89**, 243-249.
3. G. Kresse and J. Furthmuller, *Physical Review B*, 1996, **54**, 11169-11186.
4. J. P. Perdew, K. Burke and M. Ernzerhof, *Physical Review Letters*, 1996, **77**, 3865-3868.
5. G. Kresse and D. Joubert, *Physical Review B*, 1999, **59**, 1758-1775.
6. S. L. Dudarev, G. A. Botton, S. Y. Savrasov, C. J. Humphreys and A. P. Sutton, *Physical Review B*, 1998, **57**, 1505-1509.
7. Y.-L. Lee, J. Kleis, J. Rossmeisl and D. Morgan, *Physical Review B (Condensed Matter and Materials Physics)*, 2009, **80**, 224101.
8. L. Wang, T. Maxisch and G. Ceder, *Physical Review B*, 2006, **73**, 195107.
9. N. Furuhata, E. Nakamura and E. Sawaguchi, 1969.
10. J. K. Norskov, J. Rossmeisl, A. Logadottir, L. Lindqvist, J. R. Kitchin, T. Bligaard and H. Jonsson, *The Journal of Physical Chemistry B*, 2004, **108**, 17886-17892.
11. I. C. Man, H.-Y. Su, F. Calle-Vallejo, H. A. Hansen, J. I. Martínez, N. G. Inoglu, J. Kitchin, T. F. Jaramillo, J. K. Nørskov and J. Rossmeisl, *Chem. Catal. Chem.*, 2011, **3**, 1159-1165.
12. K. A. Persson, B. Waldwick, P. Lazic and G. Ceder, *Phys. Rev. B*, 2012, **85**, 235438.
13. I. Castelli, K. Thygesen and K. Jacobsen, *Top. Catal.*, 2014, **57**, 265-272.
14. E. H. P. Cordfunke and R. J. M. Konings, *Thermochimica Acta*, 2001, **375**, 65-79.
15. M. Risch, F. Ringleb, M. Kohlhoff, P. Bogdanoff, P. Chernev, I. Zaharieva and H. Dau, *Energy Environ. Sci.*, 2015, **8**, 661-674.
16. J. B. Gerken, J. G. McAlpin, J. Y. C. Chen, M. L. Rigsby, W. H. Casey, R. D. Britt and S. S. Stahl, *J. Am. Chem. Soc.*, 2011, **133**, 14431-14442.
17. J. G. McAlpin, Y. Surendranath, M. Dincǎ, T. A. Stich, S. A. Stoian, W. H. Casey, D. G. Nocera and R. D. Britt, *J. Am. Chem. Soc.*, 2010, **132**, 6882-6883.